nature communications

Article

https://doi.org/10.1038/s41467-024-53048-0

Machine learning-assisted amidase-catalytic enantioselectivity prediction and rational design of variants for improving enantioselectivity

Received: 26 February 2024

Accepted: 30 September 2024

Published online: 10 October 2024

Check for updates

Zi-Lin Li[1,2,6], Shuxin Pei[3,6], Ziying Chen[3], Teng-Yu Huang[1,2], Xu-Dong Wang[1], Lin Shen[3,4] ✉, Xuebo Chen[3,4,5] ✉, Qi-Qiang Wang[1,2], De-Xian Wang[1,2] & Yu-Fei Ao[1,2] ✉

Biocatalysis is an attractive approach for the synthesis of chiral pharmaceuticals and fine chemicals, but assessing and/or improving the enantioselectivity of biocatalyst towards target substrates is often time and resource intensive. Although machine learning has been used to reveal the underlying relationship between protein sequences and biocatalytic enantioselectivity, the establishment of substrate fitness space is usually disregarded by chemists and is still a challenge. Using 240 datasets collected in our previous works, we adopt chemistry and geometry descriptors and build random forest classification models for predicting the enantioselectivity of amidase towards new substrates. We further propose a heuristic strategy based on these models, by which the rational protein engineering can be efficiently performed to synthesize chiral compounds with higher ee values, and the optimized variant results in a 53-fold higher *E*-value comparing to the wild-type amidase. This data-driven methodology is expected to broaden the application of machine learning in biocatalysis research.

Owing to the high efficiency, excellent selectivity and environmentally benign reaction conditions, biocatalysis and biotransformation have become an important and powerful strategy in asymmetric synthesis[1–6]. Along with the increasing discovery of new enzymes and the development of protein engineering strategies, substrate scope and catalytic performance for biocatalysis are improving. However, the conventional "trial-and-error" protocol of biocatalysis research is very laborious and requires extensive experience of researchers[7–9]. It usually spends several months or even years on the discovery and engineering of a satisfactory biocatalyst.

Among the various reaction functions of biocatalysis, enantioselectivity has received almost the most attention[10,11]. Prediction on the enantioselectivity of a protein toward a target substrate will be able to greatly accelerate the establishment of a biocatalytic reaction system. Although a number of computational methods[7–14] have been developed to simulate a biocatalytic reaction, efforts to predict the enantioselectivity of biocatalysis usually fail because a small free energy difference out of the valid accuracy range of widely-used computational method can lead to a large change in enantiomeric excess values[1]. Further improvement in the accuracy

[1]Beijing National Laboratory for Molecular Sciences, CAS Key Laboratory of Molecular Recognition and Function, Institute of Chemistry, Chinese Academy of Sciences, Beijing, China. [2]University of Chinese Academy of Sciences, Beijing, China. [3]Key Laboratory of Theoretical and Computational Photochemistry of Ministry of Education, College of Chemistry, Beijing Normal University, Beijing, China. [4]Yantai-Jingshi Institute of Material Genome Engineering, Yantai, China. [5]Shandong Laboratory of Yantai Advanced Materials and Green Manufacturing, Yantai, China. [6]These authors contributed equally: Zi-Lin Li, Shuxin Pei. ✉e-mail: lshen@bnu.edu.cn; xuebochen@bnu.edu.cn; aoyufe@iccas.ac.cn

of free energy calculation requires unaffordable computational expense.

In recent years, machine learning (ML) has emerged as a powerful and effective tool for biocatalytic property prediction and protein engineering[15–28]. The success of a ML predictor depends critically on data acquisition and feature extraction. A large amount of protein sequence/structure information and biocatalysis-related reaction kinetic parameters can be obtained from open-source databases (e.g., PDB[29], UniProt[30] and BRENDA[31]). However, the lack of information on biocatalytic enantioselectivity as well as the difficulty of enantioselectivity data measurement has seriously impeded the ML study of enzyme enantioselectivity. To our best knowledge, only a few ML predictors have been reported to establish the relationship between reaction enantioselectivity and enzyme sequence/structure, including an epoxide hydrolase[32], a nitric oxide dioxygenase[33], an imine reductase[34], an amine transaminase[35] and an ene-reductase[36]. Although these predictors enable the construction of protein fitness landscapes, the important role of substrates is usually ignored[16]. It remains a challenge to (1) collect a sufficient amount of reliable data, (2) build predictors that fully describe the relationship between substrates structure and biocatalytic enantioselectivity, and (3) effectively design enzyme variants with higher enantioselectivity assisted by ML predictors.

Amidases (EC 3.5.1.X) are a class of cofactorless enzymes capable of hydrolyzing amide groups to produce acid products. Amidase-containing microbial whole cells or isolated amidases have been widely used and have successfully hydrolyzed a large number of amide substrates, making them one of the most versatile enzymes for the potential production of pharmaceuticals and commodity chemicals, such as clausena alkaloids, aza-nucleoside analogs and chiral non-natural amino acids[37]. Since the late 1990s, using nitrile hydratase/amidase-containing *Rhodococcus erythropolis* AJ270 whole cells as a catalyst, our group have systematically investigated and reported the kinetic resolution or desymmetrization of a variety of racemic or prochiral substrates to yield a series of chiral carboxamides and carboxylic acids[38–43]. In particular, when a nitrile substrate is catalyzed in tandem by nitrile hydratase and amidase from whole cells, the nitrile hydratase typically exhibits rather low enantioselectivity, while the amidase shows dominant enantioselectivity. The ee values of the products of these biotransformations therefore faithfully reflect the enantioselectivity of the amidase. Such continuous explorations also provide hundreds of reliable and comparable data for the building of corresponding machine learning model.

Herein we report ML classification models based on our collected data as well as "chemistry" and "geometry" descriptors to establish the underlying relationship between substrate structure and reaction enantioselectivity. This model is capable of predicting amidase-catalytic enantioselectivity towards new substrates and thus can be used for rapid feasibility assessment of reaction route in a heuristic way. With the help of ML, we also characterized the substrate structure and catalytic property relationship and successfully applied it to the rational design of variants for better catalytic enantioselectivity (Fig. 1).

Results and discussion

Data collection

Firstly, we summarized and collected the reactions of 240 substrates catalyzed by *Rhodococcus erythropolis* AJ270 in our previous research, including 160 kinetic resolution reactions and 80 desymmetrization reactions. Most of the reactions have been reported in journals[38–43], while a small number of reactions with negative results have been published in PhD theses (See Supplementary Source Data). In order to standardize the enantioselectivity characterization of kinetic resolution reactions and desymmetrization reactions, the ee values of products and/or the recovered substrates were transformed to E (Enantiomeric ratio) values[44] and then represented by $\Delta\Delta G^{\neq}$ according to $\Delta\Delta G^{\neq} = -RT\ln E$. All attempts to construct a regression model failed, giving a poor R^2 value as 0.354 on the test set (see Figure S2, SI). It is not surprising on account of the relatively small size of the present dataset, which is prone to the overfitting problem. The classification model was therefore considered for further research. All reactions in the dataset were classified into "positive" and "negative" based on whether the values of $-\Delta\Delta G^{\neq}$ were larger than (or equal to) 1.86, 2.40 or 3.00 kcal/mol (corresponding to ee values of products equal to 80%, 90% or 95% at 303 K, respectively). For example, under the criterion of 2.40 kcal/mol, 143 samples with $-\Delta\Delta G^{\neq} \geq 2.40$ kcal/mol were defined as positive, and the remaining 97 samples were negative.

Model training

Two types of descriptors developed by Barnard et al.[45] were adopted in this work. The first type can be obtained according to a vocabulary of molecular "cliques" that were derived from the molecular structure of substrate[46]. The second type can be calculated as the histograms of

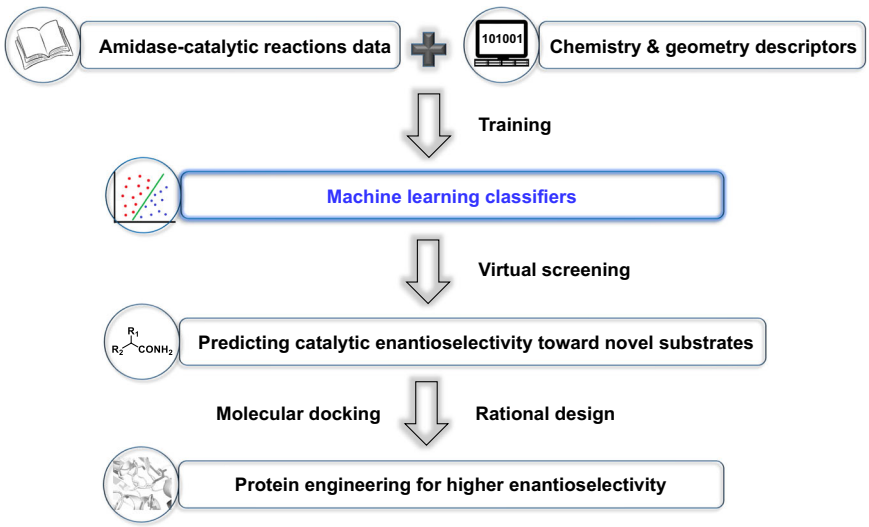

Fig. 1 | Workflow of machine learning-assisted amidase-catalytic enantioselectivity prediction and rational design of variants. This workflow includes several key steps: data collection and feature engineering, model training, virtual screening, and rational design of protein variants. Machine learning classifiers are labeled in blue color.

Table 1 | Performance of RF classifiers under different classification criteria

RF-classifiers	criterion ($-\Delta\Delta G^{\neq}$ in kcal/mol)	ee (%)	number of selected features	accuracy	recall	precision	*F*-score	AUC
Classifier A	1.86	80	56	0.978[a]	0.993	0.976	0.984	0.997
				0.784[b]	0.903	0.801	0.831	0.768
Classifier B	2.40	90	62	0.980[a]	0.990	0.977	0.983	0.998
				0.790[b]	0.859	0.809	0.831	0.832
Classifier C	3.00	95	47	0.937[a]	0.936	0.910	0.922	0.987
				0.751[b]	0.739	0.676	0.788	0.701

[a]Performance matrices of training set (similarly hereafter); [b] Performance matrices of test set (similarly hereafter). RF: Random Forest, AUC: the area under receiver operating characteristic curve.

weighted atomic-centered symmetry functions[47,48]. The former is more relevant to the chemistry information about functional groups of substrates, and the latter focuses on the three-dimensional geometry of substrates. A feature selection process was implemented in prior to training. Four classification models, that is, random forest (RF), support vector machine (SVM), logistics regression (LR), and gradient boosted decision tree (GBDT), were built on the basis of five-fold cross-validation. Their performance was evaluated based on the accuracy, precision, recall, *F*-score and the area under receiver operating characteristic curve (AUC). All ML algorithms were performed with the Scikit-learn library[49]. The geometry optimizations on substrates were implemented with Gaussian 09 software package[50].

The performance of different ML classifiers were listed in Table S3. RF, LR and GBDT are able to achieve *F*-scores above 0.8 on the test set under the classification criterion of 2.40. On account of the highest *F*-score and the smallest number of selected descriptors, the RF classifier was employed hereafter and rebuilt under other criteria. In order to check the robustness of ML predictions, 30 RF classifiers with different random seeds were rebuilt under each criterion. The results were collected in Table 1. It can be seen that the performance was good under the criteria of 1.86 and 2.40, but the *F*-score decreased below 0.8 under the criterion of 3.00. It is far from perfect but still acceptable in this work, since the ML classifier acts as a heuristic tool in prior to experiments. Two rigorous data splitting strategies were further applied by leaving all molecules involving bromine (denoted as "strategy 1") or a five-membered ring (denoted as "strategy 2") out of the training set. The ML classifier under either of these two splitting schemes can achieve an acceptable level of accuracy (Table S4).

Feature importance analysis

The feature importance can be analyzed based on the mean decrease in impurity (MDI)[51] of RF classifiers as well as the SISSO feature compositions[52] that distinguish positive reactions (higher enantioselectivity) from negative ones (lower enantioselectivity). The raw data of MDI and SISSO were shown in Figs. S3 and S4, respectively. For example, it can be seen in Figure S4(b) that a substrate with large values of three specific descriptors (denoted as SFR54, SFR69 and SFR94) has a higher tendency to be "positive", that is, $-\Delta\Delta G^{\neq} \geq 2.40$ kcal/mol and ee ≥ 90%. Some descriptors extracted by SISSO such as SFR55, SFR94 and SFR54 also appear in Figure S3, which agrees well with the feature importance analyzes based on MDI.

Most of important features belong to the atomic-centered symmetry functions (ACSFs). Based on the raw data, we further explored chemical information, that is, which functional groups or fragments are more relevant to the enantioselectivity of reactions, by mapping the extracted ACSFs to the pre-defined type of atoms[53,54] at the center. More computational details can be seen in Algorithm S1 and Table S5, SI. As shown in the importance scores in Figure S5, some specific atom types, such as the H bonded to aliphatic C with 2 electron-withdraw groups, the aliphatic sp2 N with two connected atoms, and the sp3 C in square systems, may have more significant impact on the biocatalytic enantioselectivity of substrates.

Prediction and testing toward new substrates

To demonstrate the ability of machine learning models to assist in the construction of enantioselective amidase catalytic system for the preparation of important chiral pharmaceuticals, we chose racemic 2-hydroxy-2-phenylacetamide **1a** and meso cyclopentane-1,2-dicarboxamide **3** as model substrates, which can be biocatalyzed to chiral mandelic acids[55] and disubstituted cyclopentane[56], respectively. Three classifiers under different classification criteria were used together to predict the range of $-\Delta\Delta G^{\neq}$ for a given substrate. Substrate **3** (Fig. 2B) was predicted to have a probably high enantioselectivity of this reaction, that is, $-\Delta\Delta G^{\neq} \geq 3.00$ kcal/mol. On the contrary, the prediction result of substrate **1a** (Fig. 2A) was $-\Delta\Delta G^{\neq} < 1.86$ kcal/mol, implying the potentially low ee values of its product.

To validate the accuracy of these predictions, we synthesized and experimentally measured the ee values of their reaction products. Substrates **1a** and **3** were readily prepared from simple compounds according to the literature method (see SI). Wild-type amidase-containing *Escherichia coli* whole cells were able to efficiently catalyze the kinetic resolution of the substrate **1a** within 5 min under very mild conditions (neutral phosphate buffer, 30 °C). To facilitate the isolation and detection of the product, the carboxylic acid was alkylated with benzyl bromide under base conditions and finally the recovered amide **1a** and benzyl ester **2a** were obtained with ee values of 61% and 52%, respectively, resulting in $-\Delta\Delta G^{\neq}$ of only 1.05 kcal/mol (Fig. 2A). Following a similar approach, the desymmetrization of substrate **3** gave benzyl ester **4** with 97% ee value, indicating that the $-\Delta\Delta G^{\neq}$ value of this reaction is up to 3.39 kcal/mol (Fig. 2B). Both of the above experimental results were in agreement with ML predictions, which demonstrates the reliability of our constructed predictor. It is able to significantly reduce the time for substrate synthesis and biotransformation experiments compared to the conventional research strategy.

Virtual screening

The core of conventional protein engineering approaches to enhance the poor enantioselectivity biocatalysis toward **1a** is protein engineering based on directed evolution and high-throughput screening. Instead, our strategy in the present work focuses on the substrates at the beginning and consists of two steps. First, the ML predictor is used to predict the enantioselectivity toward a series of substrates with a similar structure to **1a**. The ensemble of 30 individual RF classifiers, each of which was rebuilt with a different random seed, was applied under each classification criterion. The result was labeled as positive when more than half of the predictions were positive, otherwise it was labeled as negative. Based on the diverse results obtained using ML, we would carefully examine the substituent effect on the substrates,

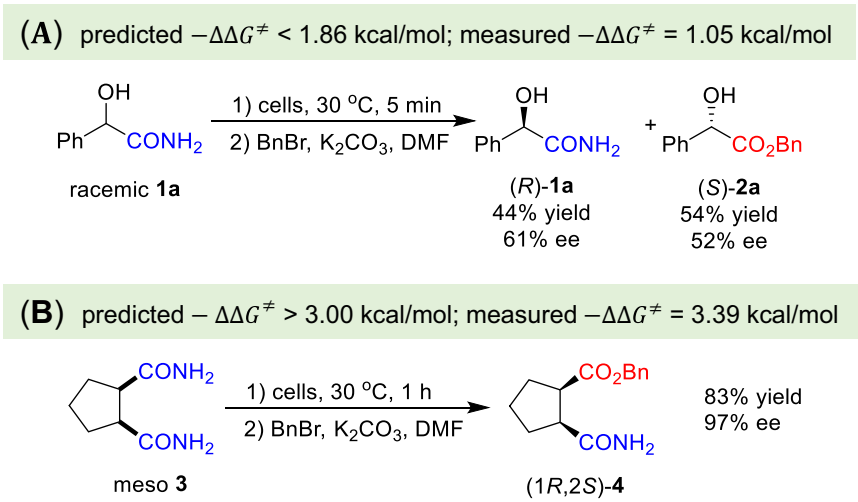

Fig. 2 | Comparison of model predictions with experimental measurements towards new substrates. Predicted and measured results of biocatalysis of substrates **1a** (**A**) and **3** (**B**). The detailed experimental procedures are given in SI. Amide groups are labeled in blue and carboxylic acid ester groups are labeled in red.

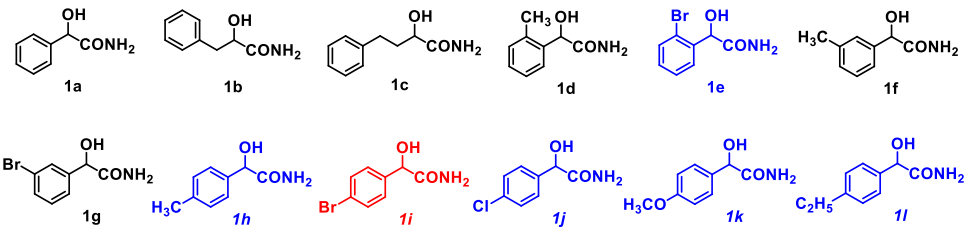

substrate	Classifier A	Classifier B	Classifier C
1a			
1b			
1c			
1d			
1e			
1f			
1g			
1h			
1i			
1j			
1k			
1l			

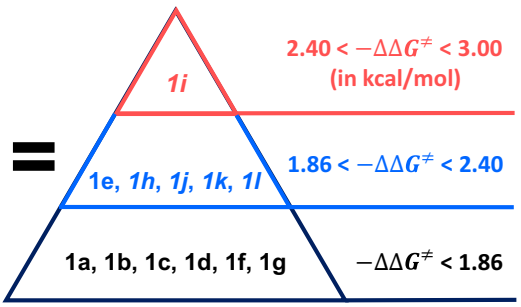

Fig. 3 | ML prediction of biocatalytic enantioselectivity toward substrates 1a-l. Positive and negative results are represented in gray and white grids, respectively. The labels of *para*-substituented substrates are highlighted in italics. Substrates with predicted $-\Delta\Delta G^{\neq}$ values < 1.86, between 1.86 and 2.40, between 2.40 and 3.00 are labeled in black, blue and red, respectively.

expecting to reveal the key factors that influence the enantioselectivity. Second, the rules revealed for the effect of substituents on enantioselectivity can be applied to assist in rational design of protein variants, which in traditional asymmetric synthesis methodologies usually require extensive wet laboratory experimental studies to reveal[38,40], thus reducing the need for mutation and screening efforts. Specifically, the aromatic group of substrate **1a** is the key site for chiral recognition with amidase. In order to comprehensively investigate the effect of the aromatic group on the catalytic performance of biocatalysis, we fine-tuned the structure of the aromatic group on **1a** to design its chemical analogs **1b**-**l** (Fig. 3).

The results in the first step are summaried in Fig. 3. When the phenyl group of **1a** was replaced by benzyl (**1b**) or phenylethyl group (**1c**), the ML-predicted values of enantioselectivity of both remain low ($-\Delta\Delta G^{\neq}$ < 1.86 kcal/mol). To investigate the effect of substituents attached on the phenyl ring, a series of substrates **1d**-**i** containing an electron-donating methyl group or an electron-withdrawing bromine group in the *ortho*-, *meta*- or *para*-position were virtually designed. According to ML predictions, the substrate **1h** with a methyl substituent in the *para*-position of the phenyl group exhibits a higher enantioselectivity ($-\Delta\Delta G^{\neq}$ > 1.86 kcal/mol) in comparison with the *ortho*- and *meta*-substituted analogs (**1e** and **1f**). Furthermore, the substrate **1i** with a *para*-bromo substituent achieves the highest predicted $-\Delta\Delta G^{\neq}$ value, which is larger than 2.40 kcal/mol. The tendency suggests that substituents in the *para*-position may be relevant to high enantioselectivity. Three additional substrates **1j**-**l** with a *para*-substituent were further examined. The ML-predicted values of $-\Delta\Delta G^{\neq}$ were both larger than 1.86 kcal/mol, leading to better enantioselectivity again when the *para*-position of the phenyl group of substrate **1** contains a substituent.

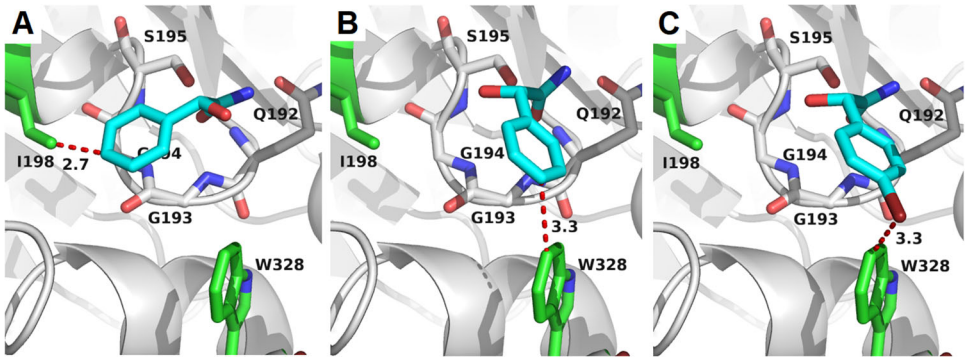

Fig. 4 | Molecular docking studies based on virtual screening results. Molecular docking of the substrate (*R*)−**1a** (**A**), (*S*)−**1a** (**B**) and (*S*)−**1i** (**C**) into the active site of amidase. protein in white cartoon, oxygen in red, nitrogen in blue, residues I198 and W328 in green, and carbon of substrates in cyan. The key interatomic distances are highlighted by red dashed lines with values. The figure was created using *PyMOL*[67].

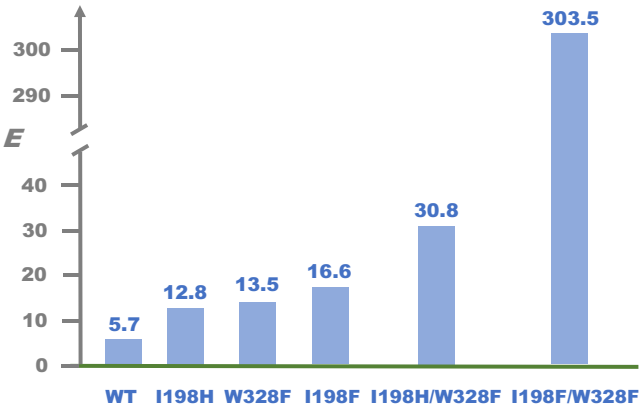

Fig. 5 | Measured *E* values of biocatalysis toward substrate 1a by amidase variants. The *E* values are displayed above the bars, while the variants are labeled below. The detailed data was shown in Table S7.

Molecular docking and rational design

To bridge the impact of *para*-substituents of substrates on stereoselectivity and the design of enzyme variants with higher enantioselectivity, we performed molecular docking of (*R*)- and (*S*)-enantiomers of substrate **1a** or **1i** into the catalytic cavity of amidase. The computational details of molecular docking can be seen in Section 4, SI. As shown in Fig. 4A, B, substrates (*R*)−**1a** and (*S*)−**1a** exhibits different binding modes, in which the *para*-position of (*R*)−**1a** and (*S*)−**1a** are close to residue I198 and W328 with a distance of 2.7 and 3.3 Å, respectively. This steric blocking was unfavorable for substrate-enzyme recognition. Similar to the binding mode of (*S*)−**1a**, the steric phenyl group of (*S*)−**1i** also extends into the substrate tunnel with a distance to W328 as 3.3 Å (see Fig. 4C). However, substrate (*R*)−**1i** failed to dock into the catalytic cavity, suggesting that its steric para-substituted phenyl group may be too close to I198 to form the similar binding mode of (*R*)−**1a**. Molecular docking of the (*R*)- and (*S*)-enantiomers of other substrates **1b-l** into the catalytic cavity of amidase also demonstrated similar binding rule (Figure S8). It inspires us to mutate residue I198 and/or W328 of amidase to enhance its enantioselectivity toward substrate **1a**, which is the key point to the second step of our rational-design strategy.

Protein engineering

Following the above biocatalysis rules, we implemented protein mutation to shrink its binding cavity of (*R*)−**1a** (residue I198) or to broaden its binding cavity of (*S*)-**1a** (W328). Three variants encoding for the substitutions I198H, I198F, and W328F of wild-type amidase were first created. The hydrolase of racemic **1a** was then measured and shown in Fig. 5. All variants displayed higher enantioselectivity with increasing *E*-values (5.7 for wild-type, 12.8 for I198H, 16.6 for I198F, 13.5 for W328F). Moreover, the double variant I198F/W328F performed the best enantioselectivity with a 53-fold higher *E*-value (i.e., 303.5) in comparison with the wild-type amidase. With the help of ML prediction of the enantioselectivity of substrates and the deep analysis based on molecular docking, we finally designed new variants and effectively achieved a dramatic increase in the enantioselectivity of amidase-catalysis.

Wet experimental validation toward new substrates

In the end, we experimentally measured the hydrolytic enantioselectivity toward substrates **1b-k** to confirm the accuracy of ML. As listed in Table 2, most of experimental results (9 out of 12) are consistent with ML predictions shown in Fig. 3. The enantioselectivity of substrates **1e** and **1 l** was overestimated, whereas the enantioselectivity of **1 h** was underestimated. The incorrect prediction regarding **1 h** and **1 l** may be related to the proximity of their measured $-\Delta\Delta G^{\neq}$ values (2.02 kcal/mol for **1 h** and 1.83 kcal/mol for **1 l**) to the classification threshold (1.86 kcal/mol) of ML predictor. The disagreement has no influence on the structure-property relationship of substrates observed by ML. Regardless, the present ML model is able to capture biocatalysis rules such as the beneficial effect of the *para*-substituents on enantioselectivity, which further assists us in rational protein engineering for highly enantioselective biocatalytic synthesis of chiral compounds.

There is still much room to improve this research in our future work. One is how to enhance and exploit the interpretability of features used in machine learning. In protein engineering and enzyme design, the chemical composition and stereostructure of substrates typically have a critical impact on the reaction, making interpretable features essential[26,57]. Some other descriptors, which have been encoded using deep neural networks[58,59] or designed for organic catalytic reactions' enantioselectivity[60], can be employed as better candidates in our future works. In the present research, however, more attention is paid to improve the traditional variant design strategy based on wet experiments and substrate engineering[38,40], and rationally designing enzyme variants through ML-assisted virtual screening of substrates, which requires a set of features with good and balanced performance. Therefore, we applied a specific combination of chemical descriptors and 3D geometry descriptors. Another is how to collect and integrate data and features involving amidase variants into existing ML models, so as to build/upgrade them to ML models describing the correlation between substrates structure, variants structure and catalytic stereoselectivity, and to explore their application in accelerating protein engineering studies.

Table 2 | Measured results of biocatalytic hydrolysis of substrates[a]

Entry	Substrate	Product 1 (%)[b](ee %)[c]	Product 2 (%)[b](ee %)[c]	$-\Delta\Delta G^{\neq}$ (kcal/mol)
1	**1a**	(*R*)-**1a** (44) (61)	(*S*)-**2a** (54) (52)	1.05
2	**1b**	(*R*)-**1b** (57) (36)	(*S*)-**2b** (25) (74)	1.35
3	**1c**	(*R*)-**1c** (52) (64)	(*S*)-**2c** (30) (80)	1.72
4	**1d**	(*R*)-**1d** (45) (25)	(*S*)-**2d** (50) (24)	0.43
5	**1e**	(*R*)-**1e** (48) (15)	(*S*)-**2e** (49) (13)	0.24[d]
6	**1 f**	(*R*)-**1f** (42) (81)	(*S*)-**2f** (51) (40)	1.01
7	**1 g**	(*R*)-**1g** (41) (91)	(*S*)-**2g** (52) (62)	1.54
8[e]	**1 h**	(*R*)-**1h** (50) (59)	(*S*)-**2h** (35) (88)	2.02
9	**1i**	(*R*)-**1i** (47) (90)	(*S*)-**2i** (37) (91)	2.52
10	**1j**	(*R*)-**1j** (50) (51)	(*S*)-**2j** (31) (91)	2.14
11	**1k**	(*R*)-**1k** (47) (70)	(*S*)-**2k** (32) (91)	2.28
12	**1 l**	(*R*)-**1l** (50) (59)	(*S*)-**2l** (32) (84)	1.83[d]

[a]substrate 1 (0.5 mmol) was incubated with amidase-containing *Escherichia coli* whole cell (0.5 g wet weight) in neutral phosphate buffer (0.1 M, 50 mL), and then was incubated at 30 °C. The detailed data was shown in Table S7. [b]Isolated yield. [c]Determined by chiral HPLC analysis, and the detailed data was shown in Table S8. [d]Mismatch with the predicted results. [e]To assign the absolute configuration, a high-quality of single crystal of the recovered **1 h** was obtained by slow evaporation of the solution in a mixture of hexane and ethyl acetate. X-ray diffraction analysis unambiguously revealed the *R*-configured stereogenic center in **1 h** (Figure S10, Table S9-10). The composition of single crystal has been proved by HPLC.

In conclusion, based on the collection of experimental biocatalytic data and the well-adopted descriptors of substrates, we have developed machine-learning classification models to predict the amidase-catalytic enantioselectivity toward new substrates. We further applied it to investigate the key structural factors of enantioselectivity and demonstrated the observed structure-property rule in the guiding of reaction route design and protein variants design. We believe that this study will shed light on the ML-assisted substrate design and protein engineering in biocatalysis.

Methods

Materials

All the restriction enzymes were purchased from Thermo Fisher Scientific. High fidelity PCR DNA-polymerase, and dNTPs were purchased from Vazyme Biotech Co., Ltd. PCR primers were synthesized and DNA sequencing was conducted by TsingKe Biotech Co., Ltd. Other common biochemical and media components were obtained from standard commercial sources and used directly. The plasmid pET22b for amidase expression is gifted from Yapeng Chao and Shijun Qian from Institute of Microbiology, Chinese Academy of Sciences. All the biochemical and commercial chemicals were used without further purification. The protocol of the synthesis of substrates and characterization data of compounds are given in SI.

Dataset Construction

The whole dataset was classified into "positive" (higher enantioselectivity) and "negative" (lower enantioselectivity) according to $\Delta\Delta G^{\neq}$, which is the difference of activation Gibbs free energies between two processes for the generation of *R*- and *S*-products. Three classification criteria, $-\Delta\Delta G^{\neq} = 1.86$, 2.40 or 3.00 kcal/mol (corresponding to ee = 80%, 90% or 95% at 303 K), were used in this work. The numbers of positive and negative samples were listed in Table S1. The dataset under each criterion was respectively divided into training (80%) and test sets (20%) with stratified random sampling. In order to address the class imbalance problem, we performed a random oversampling method to randomly duplicate samples in the minority class before ML training.

Descriptors

One type of descriptors was derived from the molecular structure of substrates. First, the whole structure was represented by the SMILES string and decomposed into fragments, which was also called as "cliques". Second, a vocabulary of molecular cliques can be created. As shown in Figure S1, there are 32 cliques extracted from this dataset and indexed as the *i*-th clique ($i = 1, 2, \ldots, 32$). Finally, a 32-dimensional one-hot vector was defined and converted into 32 descriptors. For a given compound, the *i*-th component of the vector represents the number of the *i*-th clique that appears in this molecule.

Another type of descriptors was obtained based on the weighted atomic-centered symmetry functions (wACSFs). The radial and angular wACSFs centered at atom *i* are defined as

$$W_i^{rad} = \sum_{j \neq i} Z_i e^{-\eta(r_{ij}-\mu)^2} f_{ij} \tag{1}$$

$$W_i^{ang} = \sum_{k \neq i,j} \sum_{j \neq i} Z_j Z_k (1 + \lambda \cos\theta_{jik}) e^{-\eta(r_{ij}-\mu)^2} e^{-\eta(r_{ik}-\mu)^2} e^{-\eta(r_{jk}-\mu)^2} f_{ij} f_{ik} f_{jk} \tag{2}$$

where r_{ij} is the distance between atom *i* and *j*, θ_{jik} is the angle that consists of atom *i*, *j* and *k*, Z_i denotes the atomic number of atom *i*, η, μ and λ are hyperparameters of symmetry functions, and f_{ij} is the cutoff function expressed as

$$f_{ij} = \begin{cases} \frac{1}{2}\left[\cos\left(\frac{\pi r_{ij}}{R_c}\right) + 1\right] & \text{if } r_{ij} \le R_c \\ 0, & \text{otherwise} \end{cases} \tag{3}$$

Here R_c is the pre-defined cutoff radius, which was 6.0 Å in this work; the value of λ was set as 1 or −1 for different angular symmetry functions; η and μ were determined as

$$\eta = \frac{1}{2(\Delta r)^2} \tag{4}$$

and

$$\mu = 0.5\ \text{Å} + n\Delta r, n = 0,1,2\ldots,N-1 \quad (5)$$

where

$$\Delta r = \frac{R_c - 1.5\ \text{Å}}{N-1} \quad (6)$$

and N is the number of wACSFs centered at atom i. Note that different values of N can be applied to radial and angular symmetry functions, denoted as N_{rad} and N_{ang}, respectively. Since different substrates in the dataset usually have different numbers of atoms or elements, a histogram scheme is used to regularize symmetry functions, leading to the histogram-wACSFs as "geometry" descriptors. The number of bins to build the histogram is another hyperparameter (denoted as N_{bin}).

In brief, the molecular clique descriptors reflect the "chemistry" of substrates, while the histogram-wACSF descriptors capture the three-dimensional information about substrates. Three hyperparameters in histogram-wACSFs, that is, N_{rad}, N_{ang} and N_{bin}, should be tuned. The geometry of substrate was optimized in vacuum using the B3LYP density functional[61–63] and 6-31++G(d,p) basis set. Note that "descriptor" was also called as "feature" in this paper.

Feature selection

Feature selection in prior to ML training was designed as follows. First, the features with a variance lower than a given threshold (e.g., 0.025) after normalization were removed. Second, the Pearson correlation map between the remaining features was calculated. If the coefficient of a feature pair is larger than a given threshold (e.g., 0.98), one of the features is removed. Third, recursive feature elimination[64] (RFE) was performed to filter the remaining features. After several attempts, we employed support vector machine as the estimator of RFE according to the final performance of ML classification model with the selected features. This procedure was implemented under the classification criteria of 1.86 and 2.40. However, under the criterion of 3.00, the third step was omitted. Instead, after the second step, the correlation coefficients between the remaining features and the training labels were examined, removing the features with a coefficient lower than a given threshold (e.g., 0.15).

Hyperparameters

The dataset under the classification criterion of 2.40 was used to search the best hyperparameters (Table S2). First, the hyperparameters of four classifiers, that is, random forest (RF), support vector machine (SVM), logistics regression (LR), and gradient boosted decision tree (GBDT), were tuned with a five-fold cross-validated grid-search on the training set. Second, these classifiers were retrained on the training set with the above optimized hyperparameters and evaluated on the test set. The RF model was selected as the best classifier. Finally, the RF model was rebuilt under two other classification criteria (1.86 and 3.00) with the same procedure, except for the fixed hyperparameters in histogram-wACSFs (N_{rad}, N_{ang} and N_{bin}).

Evaluation on Performance

The quality of ML classifiers is always evaluated using the accuracy, precision, recall, F-score and the area under receiver operating characteristic curve (AUC) (Table S3). They are defined as

$$\text{accuracy} = \frac{TP + TN}{TP + FP + TN + FN} \quad (7)$$

$$\text{precision} = \frac{TP}{TP + FP} \quad (8)$$

$$\text{recall} = \frac{TP}{TP + FN} \quad (9)$$

and

$$F_\beta = \frac{(1+\beta^2) \times \text{precision} \times \text{recall}}{\beta^2 \times \text{precision} + \text{recall}} \quad (9)$$

Here TP, FP, FN, and TN represent the number of positive samples correctly classified, the number of negative samples that are misclassified as positive, the number of positive samples that are misclassified as negative, and the number of negative samples correctly classified, respectively. The value of β in F-score determines the relative importance of precision and recall on the evaluation. In this work, it was set to be 1 as usual. A receiver operating characteristic curve is a plot of $\frac{TP}{TP+FN}$ in function of $\frac{FP}{TN+FP}$. A larger area under this curve (AUC) indicates better classification performance.

Protein engineering and expression

The PCR mixture (50 µL) contained 25 µL 2 × Phanta Max Master Mix, 17 µL H_2O, 2 µL DMSO, 2 µL (about 50 ng) template DNA and 2 µL (about 10 µM) each primer mix. The PCR was performed as follows: (i) 98 °C, 30 s; (ii) 30 cycles: 98 °C, 10 s; 50-72 °C, 30 s; 72 °C, 0.5 min/kbp; (iii) 72 °C, 2 min. The resulting PCR product was directly treated with the kinase, ligase & *Dpn*I (KLD enzyme mix) (100 µL mL^{-1}; NEB) at room temperature for 30 minutes and then used for the transformation of chemically competent *E. coli* TOP10 cells. After confirming the introduced mutation(s) by single colonies sequence detection, the plasmids were used for the transformation into chemical competent *E. coli* BL21(DE3) cells by the heat shock method. Primers used in this work include I198H Fw (AAGGCGGATCGATCCGGCACCCGGCGGCAT), I198H Rv (CCGCAGAATGCCGCCGGGTGCCGGATCGAT), I198F Fw (AAGGCGGATCGATCCGGTTCCCGGCGGCAT), I198F Rv (CCGCAGAATGCCGCCGGGAACCGGATCGAT), W328F Fw (ATCTGCATGCTTTCCACATCTTTAACGTGATCGCC) and W328 Rv (CCGTCCGTGGCGATCACGTTAAAGATGTGGAAAG). They are also listed in Table S6.

The pre-cultures were prepared by inoculating 5 mL of Luria-Bertani (LB) broth (composed of 1% Tryptone, 1% NaCl, and 0.5% yeast extract) containing 100 µg/mL ampicillin with a single colony of *E. coli* BL21 (DE3)[65]. Following overnight incubation at 37 °C with shaking at 220 rpm, the pre-cultures were diluted 1:100 into 300 mL of LB medium supplemented with ampicillin and cultured until the optical density at 600 nm reached approximately 0.6–0.8. After cooling at 4 °C for 30 minutes, protein expression was induced by the addition of 300 µM isopropyl-β-D-thiogalactopyranoside (IPTG), followed by further incubation for 6 hours at 25 °C. The cells were collected by centrifugation at 7100 g for 5 minutes at 4 °C, and the supernatant was discarded. The cell pellets were re-suspended in phosphate buffer (0.1 M, pH 7.0) and stored at −20 °C. All resulting variant sequences were verified through DNA sequencing.

General procedure for the biotransformations of substrates 1 and 3 catalyzed by amidase-containing or variant-containing *E. coli*

In an Erlenmeyer flask (150 mL) with a screw cap a suspension of *E. coli* cells (0.05–0.5 g wet weight) in aqueous phosphate buffer (pH 7.0, 0.1 M, 25 mL) was activated at 37 °C for 0.5 h. Substrates **1a-l** or **3** (0.5 mmol) was dissolved in aqueous phosphate buffer (pH 7.0, 0.1 M, 25 mL) and added in one portion, and the resulting mixture was incubated at 37 °C with orbital shaking (220 rpm). The reaction process was monitored using TLC method. After a period of time, the reaction was quenched by removing microbial cells through a celite pad filtration. The filtration cake was washed consecutively with water (3 × 15 mL) and ethyl acetate (3 × 30 mL). The organic

phase of filtrate was separated and dried with anhydrous Na_2SO_4, and then was removed under vacuum. The residue was chromatographed on a silica gel column with ethyl acetate as the mobile phase to give amide (***R***)−**1a-l** or **3**. The aqueous phase was evaporated under vacuum, giving a waxy solid which is a mixture of acid product and salt. The residue was dissolved in DMF (5 mL) followed by the addition of K_2CO_3 (0.25 mmol, 1 equiv.) and benzyl bromide (0.5 mmol, 2 equiv.). The mixture was stirred at room temperature overnight, and the reaction was then quenched by adding water (20 mL). Extraction with ethyl acetate (3 × 15 mL) and dried over anhydrous $NaSO_4$. After removing the solvent under vacuum, the crude mixture was purified by flash column chromatography using a mixture of petroleum ether and ethyl acetate (10:1 v/v) as the mobile phase to give benzyl esters (***S***)−**2a-l** or **4**. Enantiomeric excess values were obtained from HPLC analysis using columns coated with chiral stationary phases.

Reporting summary

Further information on research design is available in the Nature Portfolio Reporting Summary linked to this article.

Data availability

All the source data generated in this study have been deposited in Supplementary Information files. The X-ray crystallographic coordinate for structure of (*R*)-**1h** reported in this study has been deposited at the Cambridge Crystallographic Data Center (CCDC), under deposition number 2224210. These data can be obtained free of charge from the Cambridge Crystallographic Data Center via www.ccdc.cam.ac.uk/data_request/cif. The supplementary methods for synthesis and characterization, crystallography, NMR, HPLC studies and additional data supporting the findings of this study are available in Supplementary Information files. The training data used in this study are provided in the Source Data File. All data are available from the corresponding author upon request. Source data are provided with this paper.

Code availability

The source code employed for generating descriptors and training ML models in this research are available at https://github.com/ZYChen33/ML-assisted-amidase-catalytic-enantioselectivity-prediction-and-rational-design and https://doi.org/10.5281/zenodo.13759700[66].

References

1. Faber, K. et al. *Biotransformations in Organic Chemistry: A Textbook, 7th,* pp 442 (Springer, Berlin, 2018).
2. Hanefeld, U., Hollmann, F. & Paul, C. E. Biocatalysis making waves in organic chemistry. *Chem. Soc. Rev.* **51**, 594–627 (2022).
3. Wu, S. et al. Biocatalysis: enzymatic synthesis for industrial applications. *Angew. Chem. Int. Ed.* **60**, 88–119 (2021).
4. Yi, D. et al. Recent trends in biocatalysis. *Chem. Soc. Rev.* **50**, 8003–8049 (2021).
5. Winkler, C. K., Schrittwieser, J. H. & Kroutil, W. Power of biocatalysis for organic synthesis. *ACS Cent. Sci.* **7**, 55–71 (2021).
6. Devine, P. N. et al. Extending the application of biocatalysis to meet the challenges of drug development. *Nat. Rev. Chem.* **2**, 409–421 (2018).
7. Buller, R. et al. From nature to industry: harnessing enzymes for biocatalysis. *Science* **382**, eadh8615 (2023).
8. Hossack, E. J., Hardy, F. J. & Green, A. P. Building enzymes through design and evolution. *ACS Catal.* **13**, 12436–12444 (2023).
9. Miller, D. C., Athavale, S. V. & Arnold, F. H. Combining chemistry and protein engineering for new-to-nature biocatalysis. *Nat. Synth.* **1**, 18–23 (2022).
10. Qu, G. et al. The crucial role of methodology development in directed evolution of selective enzymes. *Angew. Chem. Int. Ed.* **59**, 13204–13231 (2020).
11. Adams, J. P. et al. Biocatalysis: a pharma perspective. *Adv. Synth. Catal.* **361**, 2421–2432 (2019).
12. Quesne, M. G. et al. Advances in sustainable catalysis: a computational perspective. *Front. Chem.* **7**, 182 (2019).
13. Klinman, J. P., Offenbacher, A. R. & Hu, S. Origins of enzyme catalysis: experimental findings for C-H activation, new models, and their relevance to prevailing theoretical constructs. *J. Am. Chem. Soc.* **139**, 18409–18427 (2017).
14. Lonsdale, R., Harvey, J. N. & Mulholland, A. J. A practical guide to modelling enzyme-catalysed reactions. *Chem. Soc. Rev.* **41**, 3025–3038 (2012).
15. Yang, J., Li, F.-Z. & Arnold, F. H. Opportunities and challenges for machine learning-assisted enzyme engineering. *ACS Cent. Sci.* **10**, 226–241 (2024).
16. Ao, Y.-F. et al. Data-driven protein engineering for improving catalytic activity and selectivity. *ChemBioChem* **25**, e202300754 (2024).
17. Markus, B. et al. Accelerating biocatalysis discovery with machine learning: a paradigm shift in enzyme engineering, discovery, and design. *ACS Catal.* **13**, 14454–14469 (2023).
18. Kouba, P. et al. Machine learning-guided protein engineering. *ACS Catal.* **13**, 13863–13895 (2023).
19. Dou, B. et al. Machine learning methods for small data challenges in molecular science. *Chem. Rev.* **123**, 8736–8780 (2023).
20. Wittmund, M., Cadet, F. & Davari, M. D. Learning epistasis and residue coevolution patterns: current trends and future perspectives for advancing enzyme engineering. *ACS Catal.* **12**, 14243–14263 (2022).
21. Jiang, Y., Ran, X. & Yang, Z. J. Data-driven enzyme engineering to identify function-enhancing enzymes. *Protein Eng. Des. Sel.* **36**, gzac009 (2023).
22. Sapoval, N. et al. Current progress and open challenges for applying deep learning across the biosciences. *Nat. Commun.* **13**, 1728 (2022).
23. Hie, B. L. & Yang, K. K. Adaptive machine learning for protein engineering. *Curr. Opin. Struct. Biol.* **72**, 145–152 (2022).
24. Lovelock, S. L. et al. The road to fully programmable protein catalysis. *Nature* **606**, 49–58 (2022).
25. Cui, Y., Sun, J. & Wu, B. Computational enzyme redesign: large jumps in function. *Trends Chem.* **4**, 409–419 (2022).
26. Xu, Y. et al. Deep dive into machine learning models for protein engineering. *J. Chem. Inf. Model.* **60**, 2773–2790 (2020).
27. Volk, M. J. et al. Biosystems design by machine learning. *ACS Synth. Biol.* **9**, 1514–1533 (2020).
28. Mazurenko, S., Prokop, Z. & Damborsky, J. Machine learning in enzyme engineering. *ACS Catal.* **10**, 1210–1223 (2020).
29. Berman, H. M. et al. The protein data bank. *Nucleic Acids Res.* **28**, 235–242 (2000).
30. UniProt Consortium, The UniProt: the universal protein knowledgebase in 2023. *Nucleic Acids Res.* **51**, D523–D531 (2023).
31. Chang, A. et al. BRENDA, the ELIXIR core data resource in 2021: new developments and updates. *Nucleic Acids Res.* **49**, D498–D508 (2021).
32. Cadet, F. et al. A machine learning approach for reliable prediction of amino acid interactions and its application in the directed evolution of enantioselective enzymes. *Sci. Rep.* **8**, 16757 (2018).
33. Wu, Z. et al. Machine learning-assisted directed protein evolution with combinatorial libraries. *Proc. Natl Acad. Sci. USA.* **116**, 8852–8858 (2019).
34. Ma, E. J. et al. Machine-directed evolution of an imine reductase for activity and stereoselectivity. *ACS Catal.* **11**, 12433–12445 (2021).
35. Ao, Y.-F. et al. Structure- and data-driven protein engineering of transaminases for improving activity and stereoselectivity. *Angew. Chem. Int. Ed.* **62**, e202301660 (2023).
36. Clements, H. D. et al. Using data science for mechanistic insights and selectivity predictions in a non-natural biocatalytic reaction. *J. Am. Chem. Soc.* **145**, 17656–17664 (2023).

37. Wu, Z. et al. Amidase as a versatile tool in amide-bond cleavage: from molecular features to biotechnological applications. *Biotechnol. Adv.* **43**, 107574 (2020).
38. Ao, Y.-F. et al. Reversal and amplification of the enantioselectivity of biocatalytic desymmetrization toward meso heterocyclic dicarboxamides enabled by rational engineering of amidase. *ACS Catal.* **11**, 6900–6907 (2021).
39. Hu, H.-J. et al. Modification of the enantioselectivity of biocatalytic *meso*-desymmetrization for synthesis of both enantiomers of *cis* –1,2-disubstituted cyclohexane by amidase engineering. *Adv. Synth. Catal.* **363**, 4538–4543 (2021).
40. Hu, H.-J. et al. Enantioselective biocatalytic desymmetrization for synthesis of enantiopure *cis*–3,4-disubstituted pyrrolidines. *Green. Synth. Catal.* **2**, 324–327 (2021).
41. Hu, H.-J. et al. Highly efficient biocatalytic desymmetrization of *meso* carbocyclic 1,3-dicarboxamides: a versatile route for enantiopure 1,3-disubstituted cyclohexanes and cyclopentanes. *Org. Chem. Front.* **6**, 808–812 (2019).
42. Ao, Y.-F. et al. Biocatalytic desymmetrization of prochiral 3-aryl and 3-arylmethyl glutaramides: different remote substituent effect on catalytic efficiency and enantioselectivity. *Adv. Synth. Catal.* **360**, 4594–4603 (2018).
43. Wang, M.-X. Enantioselective biotransformations of nitriles in organic synthesis. *Acc. Chem. Res.* **48**, 602–611 (2015).
44. Janes, L. E., Kazlauskas, R. J. & Quick, E. a fast spectrophotometric method to measure the enantioselectivity of hydrolases. *J. Org. Chem.* **62**, 4560–4561 (1997).
45. Barnard, T. et al. Less may be more: an informed reflection on molecular descriptors for drug design and discovery. *Mol. Syst. Des. Eng.* **5**, 317–329 (2020).
46. Jin, W., Barzilay, R. & Jaakkola, T. Junction tree variational auto-encoder for molecular graph generation. *Proceedings of the 35th International Conference on Machine Learning,* PMLR **80**, 2323–2332 (2018).
47. Gastegger, M. et al. wACSF—Weighted atom-centered symmetry functions as descriptors in machine learning potentials. *J. Chem. Phys.* **148**, 241709 (2018).
48. Behler, J. & Parrinello, M. Generalized neural-network representation of high-dimensional potential-energy surfaces. *Phys. Rev. Lett.* **98**, 146401 (2007).
49. Pedregosa, F. et al. Scikit-learn: machine learning in python. *J. Mach. Learn. Res.* **12**, 2825–2830 (2011).
50. Gaussian 09, Revision D.01, Frisch, M. J. et al. Gaussian, Inc., Wallingford CT, (2013).
51. Breiman, L. Random forests. *Mach. Learn.* **45**, 5–32 (2001).
52. Ouyang, R. et al. SISSO: a compressed-sensing method for identifying the best low-dimensional descriptor in an immensity of offered candidates. *Phys. Rev. Mater.* **2**, 083802 (2018).
53. Case, D. A. et al. AMBER18, University of California, San Francisco, (2018).
54. Wang, J. et al. Development and testing of a general amber force field. *J. Comput. Chem.* **25**, 1157–1174 (2004).
55. Singh, R. V. & Sambyal, K. Green synthesis aspects of (*R*)-(-)-mandelic acid; a potent pharmaceutically active agent and its future prospects. *Crit. Rev. Biotechnol.* **43**, 1226–1235 (2023).
56. Borzilleri, R. M., Weinreb, S. M. & Parvez, M. Total synthesis of the unusual marine alkaloid (-)-Papuamine utilizing a novel imino ene reaction. *J. Am. Chem. Soc.* **117**, 10905–10913 (1995).
57. Tahil, G. et al. Stereoisomers are not machine learning's best friends. *J. Chem. Inf. Model.* **64**, 5451–5469 (2024).
58. Walters, W. P. & Barzilay, R. Applications of deep learning in molecule generation and molecular property prediction. *Acc. Chem. Res.* **54**, 263–270 (2021).
59. Schütt, K. T. et al. SchNetPack 2.0: a neural network toolbox for atomistic machine learning. *J. Chem. Phys.* **158**, 144801 (2023).
60. Reid, J. P. & Sigman, M. S. Holistic prediction of enantioselectivity in asymmetric catalysis. *Nature* **571**, 343–348 (2019).
61. Becke, A. D. Density-functional exchange-energy approximation with correct asymptotic behavior. *Phys. Rev. A: ., Mol., Opt. Phys.* **38**, 3098–3100 (1988).
62. Lee, C., Yang, W. & Parr, R. G. Development of the Colle-Salvetti correlation-energy formula into a functional of the electron density. *Phys. Rev. B: Condens. Matter Mater. Phys.* **37**, 785–789 (1988).
63. Becke, A. D. Density-functional thermochemistry. III. the role of exact exchange. *J. Chem. Phys.* **98**, 5648–5652 (1993).
64. Guyon, I. et al. Gene selection for cancer classification using support vector machines. *Mach. Learn.* **46**, 389–422 (2002).
65. Xue, Z. et al. Overexpression of a recombinant amidase in a complex auto-inducing culture: purification, biochemical characterization, and regio- and stereoselectivity. *J. Ind. Microbiol. Biotechnol.* **38**, 1931–1938 (2011).
66. Li, Z.-L. et al. ML-assisted-amidase-catalytic-enantioselectivity-prediction-and-rational-design. https://doi.org/10.5281/zenodo.13759700 (2024).
67. The PyMOL molecular graphics system, version 2.3.0. Schrödinger, LLC. New York, (2019).

Acknowledgements

Financial supports from the National Key Research and Development Program of China (2019YFA0709400 to LS), the Strategic Priority Research Program of the Chinese Academy of Sciences (XDB0960302 to YFA), the National Natural Science Foundation of China (22193041 to LS, 21977098 to YFA, 22120102005 to XC) and the Fundamental Research Funds for the Central Universities to LS are gratefully acknowledged. We are grateful to Prof. Mei-Xiang Wang for providing the training data.

Author contributions

Y.F.A. and L.S. conceived the project and supervised the work with Q.Q.W., D.X.W., and X.C. Data collection and dataset building was performed by Y.F.A., S.P., T.Y.H., and X.D.W. The ML model was designed and built by S.P., Z.C., L.S., and Y.F.A. Biocatalytic experiments were performed by Z.L.L. Protein engineering was designed and performed by Y.F.A. and Z.L.L., Y.F.A., L.S., and S.P. wrote the manuscript, which was edited and approved by all authors.

Competing interests

The authors declare no competing interests.

Additional information

Supplementary information The online version contains supplementary material available at https://doi.org/10.1038/s41467-024-53048-0.

Correspondence and requests for materials should be addressed to Lin Shen, Xuebo Chen or Yu-Fei Ao.

Peer review information *Nature Communications* thanks Arkadij Kummer, Eric Ma and the other, anonymous, reviewer(s) for their contribution to the peer review of this work. A peer review file is available.